

Facile Synthesis of gC_3N_4 -Exfoliated $BiFeO_3$ Nanocomposite: A Versatile and Efficient S-Scheme Photocatalyst for the Degradation of Various Textile Dyes and Antibiotics in Water

Darshana Anand Upar, Debika Gogoi, Manash R. Das, Bhanudas Naik, and Narendra Nath Ghosh*



Cite This: *ACS Omega* 2023, 8, 38524–38538



Read Online

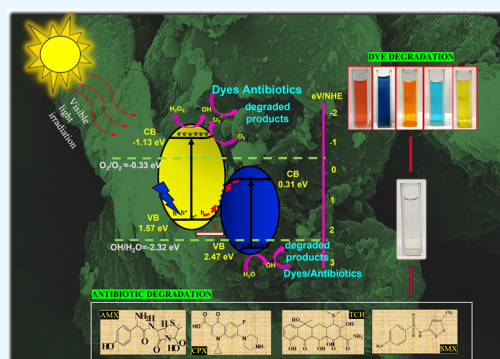
ACCESS |

Metrics & More

Article Recommendations

Supporting Information

ABSTRACT: Water pollution engendered from textile dyes and antibiotics is a globally identified precarious concern that is causing dreadful risks to human health as well as aquatic lives. This predicament is escalating the quest to develop competent photocatalysts that can degrade these water pollutants under solar light irradiation. Herein, we report an efficient photocatalyst comprising a hierarchical structure by integrating the layered graphitic carbon nitride (gC_3N_4) with nanoflakes of exfoliated $BiFeO_3$. The coexistence of these two semiconducting nanomaterials leads to the formation of an S-scheme heterojunction. This nanocomposite demonstrated its excellent photocatalytic activity toward the degradation of several textile dyes (Yel CL2R, Levasol Yellow-CE, Levasol Red-GN, Navy Sol-R, Terq-CLSB) and various antibiotics (such as tetracycline hydrochloride (TCH), ciprofloxacin (CPX), sulfamethoxazole (SMX), and amoxicillin (AMX)) under the simulated solar light irradiation. As this photocatalyst exhibits its versatile activity toward the degradation of several commercial dyes as well as antibiotics, this work paves the path to develop a reasonable, eco-benign, and highly efficient photocatalyst that can be used in the practical approach to remediate environmental pollution.



1. INTRODUCTION

Water security is inextricably linked to the sustainable development, social and economic welfare of humans, and a healthy ecosystem.¹ Global climate change and water quality are the major challenges faced in the world in the 21st century.^{2,3} The human population has grown more than three times larger than it was in the mid-twentieth century, and urbanization of this population and economic progress ensued rapid industrialization and expansion in particularly fabric, dairy, poultry, livestock farming, fish farming, food, and pharmaceuticals industries, which are the leading sources of water pollution.^{4,5} Natural and industrial water polluting agents such as dyes, chloro, and nitro phenols, antibiotics, and antibiotic-resistant bacteria are irreversible hazards to human and aquatic life and present a serious challenge for water to be suitable for environment and human use such as drinking and agricultural use, and undermine food security and contaminate the food chain. Some of the industrial synthetic dye effluents are extremely toxic, stable, and carcinogenic causing chronic poisoning, nervous system damage, and cancer.⁶ The vivid and vibrant chroma of the dyes and pigments from the effluents to the acquiring aquatic ecosystem render ecological problems, such as inhibition of benthic photosynthesis due to obstruction of sunlight.^{7–11}

Another conspicuous pollutant present in water is various types of antibiotics. The use of antibiotics and performance-

enhancing antibiotic growth promoters and antibiotic feed are an integral part of the efficient farming process in dairy, livestock, poultry, and fish farms which improves the overall health, growth, and production and prevents transmission of bacterial diseases.^{12–14} However, the uncontrolled and unregulated use of antibiotic products in farms has generated effluents containing antibiotics and impacted the fragile natural ecosystems of rivers and lakes. Another serious disadvantage of antibiotic-containing effluents is the development of antibiotic-resistant bacteria, which poses an extreme health risk and complications in humans as well as animals.^{15–18} Hence, antibiotic resistance has been considered as a major global health crisis by the World Health Organization (WHO).^{19,20}

The control and remediation of these serious water pollution problems from dyes and antibiotics require the development of wastewater treatment using economically and environmentally friendly techniques. Environmental scientists and many environmentally motivated startups have eagerly shown interest and have innovated different water treatment systems

Received: July 24, 2023

Accepted: September 27, 2023

Published: October 6, 2023



for the effective treatment of water polluting agents such as physical, chemical, hybrid, and artificial-intelligence-driven methods. Various modern wastewater treatment techniques include the use of physical methods such as adsorption, membrane filtration (nanofiltration, ultrafiltration), coagulation/flocculation), microwave (MW) irradiation, chemical methods such as and UV assisted Fenton's oxidation and ozonation, etc., and biological methods (decomposition of organic pollutants by microorganisms via aerobic or anaerobic cycle) are utilized for different wastewater treatments.⁷ However, the use of these techniques is limited due to the drawbacks associated with these techniques, such as the generation of a large volume of sludge in physical techniques, high-energy prerequisite in the membrane filtration technique, maintenance demands, and high cost; chemical methods are not economically viable for large-scale wastewater treatment and also environmentally unfriendly techniques; and biological treatment is a slow process and requires a suitable environment and specialized laboratories for the maintenance of microorganisms.^{21–29}

In this context, the use of photocatalysts to degrade the pollutants by using semiconductors (e.g., TiO_2 , ZnO , WO_3 , etc.) as catalysts appears as an alternative. However, the wide band gap energy of these abovementioned catalysts compels the UV irradiation to exhibit their photocatalytic activity. The UV light makes this process environment-unfriendly and expensive, hence limiting its large-scale applications.^{11,30–35} Although lowering the band gap energy of a semiconductor photocatalyst to make it effective under visible light seems a reasonable strategy, a low band gap also causes electron–hole recombination which makes the photocatalyst inactive.

Therefore, the ongoing quest is developing a suitable photocatalyst that is capable of demonstrating their activities under visible light or sunlight exposure.^{36–40} In this venture, band gap engineering and efficient absorption of light with a wide range of wavelength plays the decisive role. To achieve efficient photon absorption and effective excitation, semiconductor with a small band gap is preferable. However, the redox potentials of reactions should be contained between conduction band (CB) and valence band (VB) level potentials, which demand a more negative CB potential and more positive VB potential. Hence, it is expected that a photocatalyst should synchronically possess a wide light-absorption range, Coulomb field strength, efficient charge separation, and strong redox ability. However, satisfying all of these criteria by a single-component semiconductor is very difficult. Therefore, the construction of heterostructures by combining two different semiconductors, having unequal band structure, becomes an attractive strategy to achieve heterojunctions where photo-generated effective e^- and h^+ remain spatially separated and significantly restrain charge recombination. Different mechanisms have been suggested to expound the charge dynamics of different types of heterojunctions, such as Type I heterojunction, Type II heterojunction, p–n heterojunction, Schottky junction, Z-scheme heterojunction, S-scheme heterojunction, etc.^{41–50} Among various heterostructure photocatalysts, p–n heterojunctions with staggered band alignments (Type II) have gained immense interest. In the type-II heterojunction, photogenerated electrons accumulate on the CB of semiconductor-I with weak reduction potential, while photogenerated holes gather on the VB of semiconductor-II with weak oxidation potential. This electron transfer process results in the weakening of its redox ability, and the

heterojunction encounters dynamic and thermodynamic limitations. To address these issues, Yu and co-workers have proposed a novel step-scheme (S-scheme) heterojunction in 2018.⁴⁴ An S-scheme heterojunction is composed of an oxidation photocatalyst (OP) and a reduction photocatalyst (RP) with staggered band structures, which is similar to a type-II heterojunction but with a completely different charge-transfer pathway. Here, at the interface between the OP and RP, an internal electric field (IEF) is generated, which plays a critical role in the electron transfer. The important feature of this charge-transfer process is that here, the photogenerated pointless weaker reductive electrons and oxidative holes are recombined, while the powerful photogenerated electrons and holes are reserved in the CB of RP and VB of OP, respectively, and maintain an efficient charge separation and introduce a strong redox potential.^{44–46,49–51}

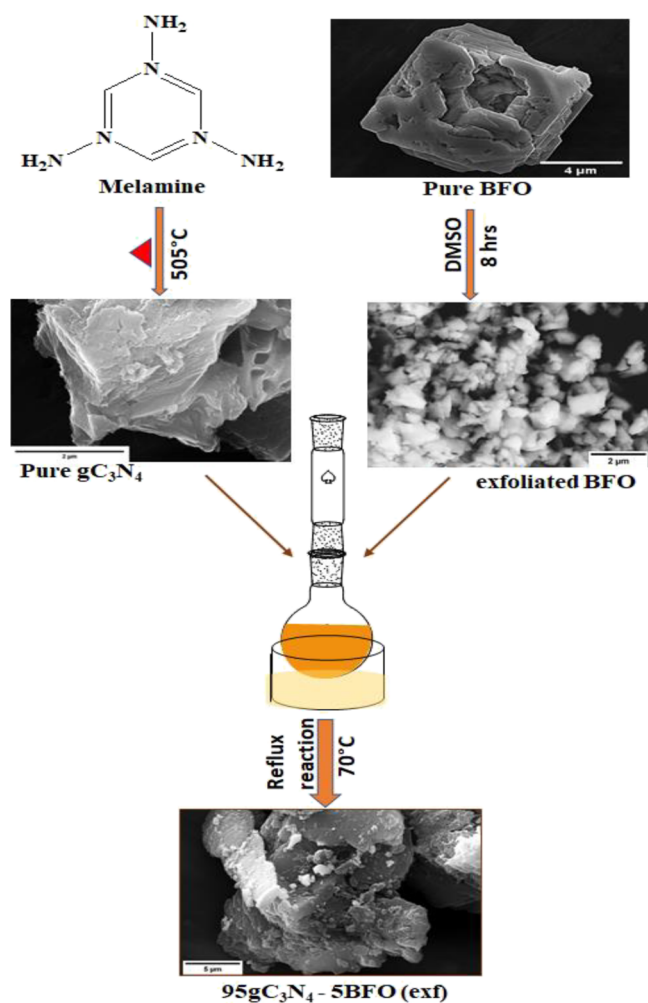
For the last couple of decades, several researchers have developed an enormous number of photocatalysts and reviews have been published discussing these photocatalysts.^{5,52–57} However, to the best of our knowledge, to date, the development of a single photocatalyst that can manifest versatile performance by effectively degrading several industrial dyes as well as various antibiotics is not yet reported. In this present work, we have designed a photocatalyst which is a nanocomposite composed of graphitic carbon nitride (gC_3N_4) and BiFeO_3 . Because the astonishing photocatalytic activity of gC_3N_4 (band gap energy ~ 2.7 eV) has attracted colossal attraction, we have chosen it as one of the components of the nanocomposite^{58–62} and enhanced its photocatalytic activity by introducing BiFeO_3 (BFO) in the composition of the nanocomposite. BFO has been chosen because of its compatible band gap (~ 2.0 – 2.7 eV),⁶¹ strong photo absorption properties, and multiferroic nature.

In this study, we report the synthesis of a nanostructured photocatalyst by anchoring BFO nanoflakes on the surface, as well as within the layers of gC_3N_4 . We have evaluated the photocatalytic activity of this catalyst toward a model dye (Rhodamine-B), several commercial dyes used in textile industries (Yel CL2R, Levasol Yellow-CE, Levasol Red-GN, Navy Sol-R and Terq-CL5B), and various antibiotics (such as tetracycline hydrochloride (TCH), ciprofloxacin (CPX), sulfamethoxazole (SMX), and amoxicillin (AMX)) under the simulated solar light irradiation. We have proposed an S-scheme heterojunction mechanism to explain the photocatalytic activity of this catalyst and also proposed the photodegradation pathways of the antibiotics.

2. EXPERIMENTAL SECTION

2.1. Synthesis of the Photocatalyst. The synthesis of the gC_3N_4 -exfoliated BFO nanocomposite is depicted in Scheme 1. To synthesize this nanocomposite, we have employed a three-step process. Step 1: Pure gC_3N_4 was synthesized by calcining melamine at 550 °C for 2 h. Step 2: BFO particles were synthesized using $\text{Bi}(\text{NO}_3)_3$ and FeCl_3 as starting materials. From an aqueous mixture of these starting chemicals, a precursor was prepared by using NaOH as the precipitating agent. This precursor was then hydrothermally treated at 145 °C for 24 h. This resulted in the formation of cubic-shaped BFO particles, which were composed of thin lamella. Then, BFO particles were exfoliated by stirring them in DMSO and obtained exfoliated BFO (BFO(exf)) having a nanoflake-like microstructure. Step 3: gC_3N_4 -BFO(exf) nanocomposites were prepared by refluxing the dispersion of pure gC_3N_4 and

Scheme 1. Synthetic Route of 95gC₃N₄-5BFO(exf) Nanocomposites



pure BFO nanoflakes in methanol, followed by drying the resultant solid at 60 °C for ~10 h. The details of the synthesis,

characterization techniques, and instrumentation are given and are provided in the [Supporting Information](#).

2.2. Photocatalysis Reaction. We have carried out the photocatalysis of different dyes (e.g., model dye (Rhodamine-B), textile industries (Yel CL2R, Levasol Yellow-CE, Levasol Red-GN, Navy Sol-R and Terq-CL5B)) and various antibiotics (such as tetracycline hydrochloride (TCH), ciprofloxacin (CPX), sulfamethoxazole (SMX), and amoxicillin (AMX)) under simulated solar light irradiation. The progress of the reaction was monitored with time by using UV-vis spectroscopy, apparent rate constant (k_{app}), and formal quantum efficiency (FQE). The details of the photocatalysis reactions are provided in the [Supporting Information](#).

3. RESULTS AND DISCUSSION

3.1. Structural Characterizations of the Synthesized Materials.

The crystalline phases and microstructures of the synthesized materials (e.g., pure gC₃N₄, BFO (unexfoliated), BFO (exfoliated), and gC₃N₄-BFO nanocomposites) were determined by performing X-ray diffraction (XRD) and field emission scanning electron spectroscopy (FESEM) study. [Figure 1a](#) displays the XRD patterns of the nanocomposite, pure gC₃N₄, pure BFO(exf), and 95gC₃N₄-5BFO(exf) nanocomposite. The XRD pattern of pure gC₃N₄ diffraction peaks at $2\theta = 13.1^\circ$ and 27.4° ^{11,63} correspond to its (100) and (002) planes.⁶⁴ The XRD pattern of BFO(exf) presents the peaks at $2\theta = 22.3^\circ, 31.7^\circ, 32.14^\circ, 38.88^\circ, 39.53^\circ, 45.8^\circ, 51.2^\circ, 51.8^\circ, 56.41^\circ, 57.03^\circ, 66.3^\circ, 67.1^\circ, 71.4^\circ, \text{ and } 76.01^\circ$ which correspond to (101), (012), (110), (003), (021), (012), (113), (211), (104), (122), (024), (220), (303), and (214) (JCPDS card no: 20-0169) and indicates its rhombohedral distorted perovskite structure with space group $R3c$ and lattice parameters of $a = b = c = 5.62043 \text{ \AA}$ and $\alpha = \beta = \lambda = 59.35381^\circ$.⁶⁵ In the case of the 95gC₃N₄-5BFO(exf) nanocomposite, the presence of peaks $2\theta = 13.1^\circ$ and 27.4° (indicating the presence of gC₃N₄) along with peaks at $2\theta = 22.1^\circ, 31.6^\circ, 39.28^\circ, 45.6^\circ, 51.2^\circ, \text{ and } 56.6^\circ$ (affirming the presence of BFO) were observed. The XRD pattern of the 90gC₃N₄-10BFO(exf) nanocomposite also shows the presence of characteristic peaks of gC₃N₄ and BFO(exf) ([Figure S1](#)).

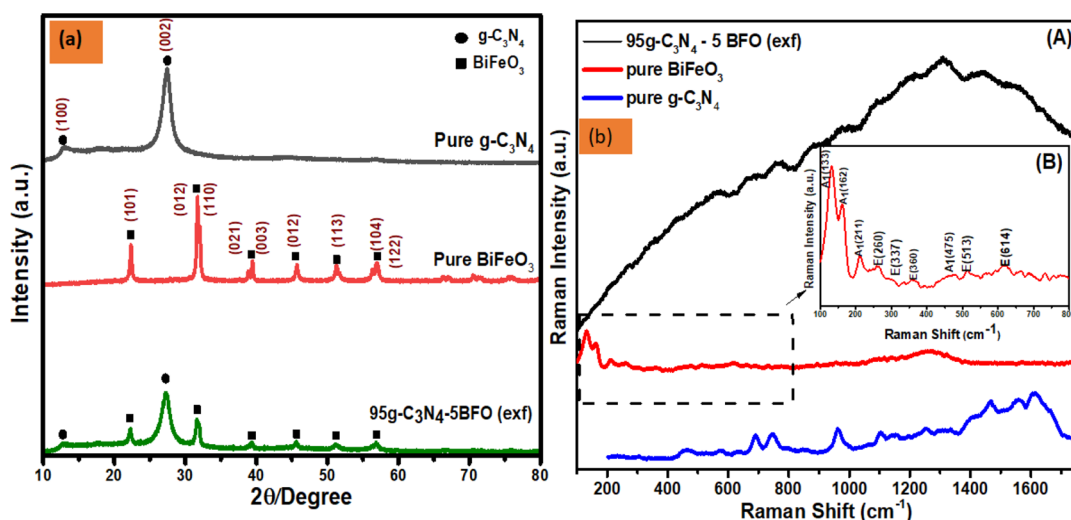


Figure 1. (a) XRD pattern of pure gC₃N₄, BiFeO₃(exf), 95gC₃N₄-5BFO(exf) nanocomposite, (b) Raman spectra of pure gC₃N₄, BiFeO₃(exf), 95gC₃N₄-5BFO(exf) nanocomposite.

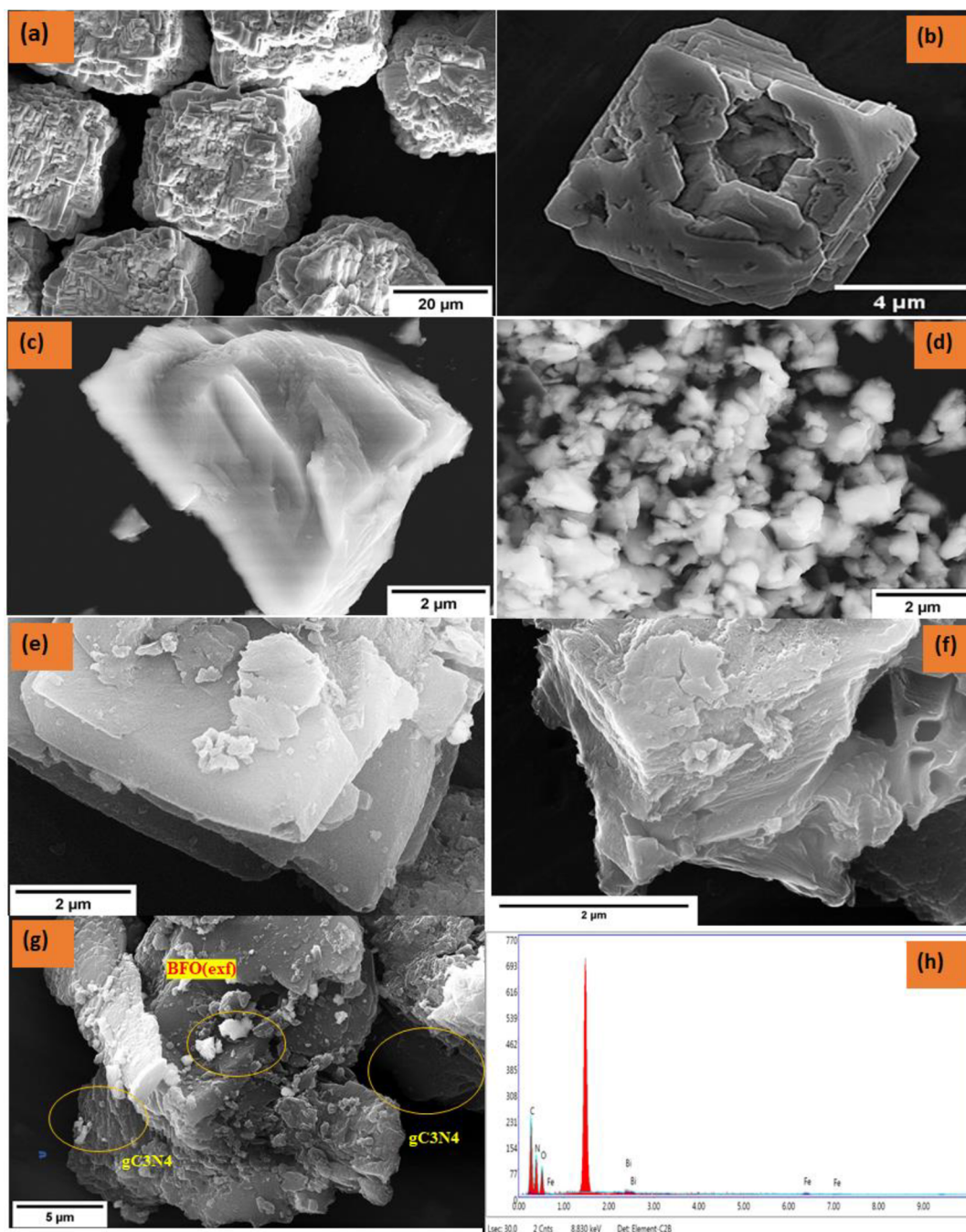


Figure 2. FESEM micrographs of (a,b) BFO, (c) early stage of BFO exfoliation, (d) nanoflakes of BFO obtained after exfoliation (BFO(exf)), (e,f) gC_3N_4 with layered structure, (g) $95gC_3N_4$ -5BFO(exf), and (h) EDX spectra of $95gC_3N_4$ -5BFO(exf) nanocomposite.

The Raman spectra of pure gC_3N_4 (Figure 1b) exhibit peaks which can be attributed to (i) layer–layer deformation vibrations or the correlation vibrations ($462, 578, 693\text{ cm}^{-1}$), (ii) out-of-plane bending mode of the graphitic domain (746 cm^{-1}), (iii) breathing mode of the s-triazine ring (963 cm^{-1}), (iv) lattice vibration of gC_3N_4 (1253 cm^{-1}), (v) D band (1465 cm^{-1}), G band (1558 cm^{-1}), and (vi) heterocyclic CN vibrations (1616 cm^{-1}).^{11,43,66–68} The Raman spectra of BFO(exf), where the appearance of phonon modes at 133, 162, 211, and 475 cm^{-1} (for A_1 modes) and at 260, 360, 475, 513, 614, and 1262 cm^{-1} (for E modes) were observed.^{69,70} $95gC_3N_4$ -5BFO(exf) exhibited a very broad spectrum where the bands at 570, 681, 756, 971, 1215, 1309, 1440, and 1574

cm^{-1} were present and indicated the presence of gC_3N_4 and BFO in the nanocomposite. However, as $95gC_3N_4$ -5BFO(exf) contains only 5 wt % BFO, the peaks for BFO were very small. In the FTIR spectra (Figure S2), the following IR bands were observed for both gC_3N_4 and $95gC_3N_4$ -5BFO(exf): (i) 1635 cm^{-1} (C=N stretching vibration), (ii) 1566 and 1414 cm^{-1} (s-triazine ring vibrations), (iii) 1326 and 1249 cm^{-1} (C–N stretching), and (iv) 801 cm^{-1} (s-triazine ring vibration).¹¹

We have investigated the microstructures of the synthesized materials by using FESEM and the micrographs are displayed in Figure 2. Figure 2a,b shows the as-synthesized unexfoliated BFO particles, which are cubical in structure, and these micrometer size cubes are formed by assembling nanometer-

thin lamella. To anchor the BFO on the surface of the C_3N_4 layers, BFO cubes were exfoliated to nanoflakes. Figure 2c shows the early stage of the exfoliation process, where the expansion of interlayer spacing occurred due to the intercalation of DMSO molecules. Finally, nanoflakes of BFO(exf) were formed as shown in Figure 2d. FESEM micrographs Figure 2e,f exhibits the stacking of nanometer-thin layers in the microstructure of gC_3N_4 . In the 95 gC_3N_4 -5BFO(exf) nanocomposite, deposition of nanoflakes of exfoliated BFO on the surface of the gC_3N_4 layers is observed in Figure 2g. In the EDS spectra of the nanocomposite (Figure 2h), the presence of peaks for C, N, O, Fe, and Bi was observed.

The HRTEM micrographs of 95 gC_3N_4 -5BFO(exf) are presented in Figure 3a. In Figure 3b, the lattice fringes

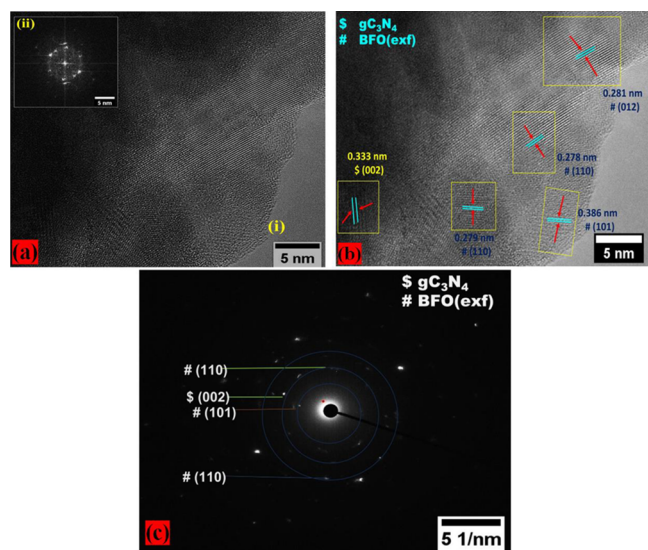


Figure 3. (a) HRTEM micrograph of the 95 gC_3N_4 -5BFO(exf) nanocomposite (inset FFT pattern), (b) the lattice fringes, and (c) SAED patterns of gC_3N_4 and BFO(exf) in the nanocomposite.

corresponding to (012), (110), and (101) planes of 5BFO(exf) and (002) plane of gC_3N_4 were observed, which confirmed the presence of BFO and gC_3N_4 in the nanocomposite. The selected area electron diffraction (SAED) pattern of the nanocomposite (Figure 3c) also exhibits the presence of characteristic diffraction spots corresponding to BFO and gC_3N_4 .

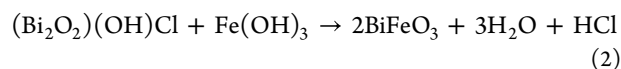
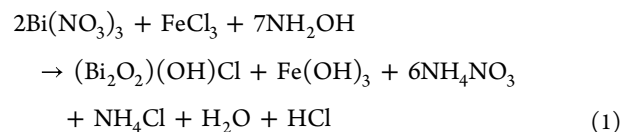
The elemental compositions and their chemical states present in the 95 gC_3N_4 -5BFO(exf) nanocomposite were studied by using XPS analysis. The obtained XPS survey spectrum is presented in Figure S3 which depicts the presence of Bi 4f, Fe 2p, O 1s, C 1s, and N 1s peaks. Figure 4a presents the high-resolution Bi 4f spectrum consisting of two intense peaks at 158.8 and 164.1 eV which correspond to Bi 4f_{7/2} and Bi 4f_{5/2}.^{71,72} This indicated the presence of Bi in its +3 oxidation state in the nanocomposite. The high-resolution Fe 2p spectra shown in Figure 4b revealed two peaks at 710.7 and 724.1 eV corresponding to Fe 2p_{3/2} and Fe 2p_{1/2} along with their corresponding satellite peaks at 717.7 and 733.2 eV.⁷³ This showed the existence of Fe³⁺. Figure 4c displays the deconvoluted O 1s spectrum, composed of two peaks at 529.6 and 532.3 eV which revealed the presence of O in two different kinds of chemical states. The peak at 529.6 eV can be attributed to the lattice oxygen (O_L) of BiFeO₃, and the peaks

at 532.3 eV can be attributed to the chemisorbed oxygen caused by oxygen vacancies (O_V) of BiFeO₃.⁷² The C 1s XPS spectrum shown in Figure 4d was deconvoluted into three peaks at 284.8, 286.4, and 288.6 eV, due to the presence of C–C, N–C=N, and C–(N)₃ bonds, respectively.^{74,75} A satellite peak was also observed at 294.2 eV as a result of $\pi\pi^*$ excitations. The high-resolution N 1s spectrum shown in Figure 4e was fitted with three peaks at 399, 400.8, and 404.7 eV which were credited to C=N–C, N–(C)₃, and N–H bonds, respectively.^{76,77}

BET surface area and BJH pore size of gC_3N_4 were determined by performing N₂ adsorption–desorption analysis. Isotherms of both the samples showed type IV isotherm with H₃ hysteresis loop indicating the nonrigid aggregates of platelike particles (Figure S4a). Although the addition of 5 wt % BFO with 95 wt % gC_3N_4 (95 gC_3N_4 -5BFO) caused a slight increase in the specific surface of gC_3N_4 (from 4.4 to 4.5 m²/g), the BET average pore diameter was increased from 120.08 to 178.23 Å (Figure S4b). This enhancement of the pore size could be due to the incorporation of BFO nanoflakes within the layered structure of gC_3N_4 .

These aforementioned characterization techniques indicate the presence of BFO and gC_3N_4 in the nanocomposite. The reaction involved in the formation of gC_3N_4 by the calcination of melamine can be presented as Scheme 2.

In the first step of the BFO synthesis, (Bi₂O₂)(OH)Cl and Fe(OH)₃ form as precipitates in the coprecipitation process. Hydrothermal treatment of these precipitates leads to the formation of BiFe₂O₃ and the reactions can be presented as eq 1 and 2.



Intercalation of DMSO within the layers of BFO resulted in the formation of nanoflakes of BFO through the exfoliation of BFO layers.

We studied the optical absorption properties of the as-synthesized materials by using UV–vis diffuse reflectance spectroscopy. Figure 4f(i) represents the UV–Vis DRS spectra and Tauc plot of pure gC_3N_4 , pure BFO(exf), and the 95 gC_3N_4 -5BFO(exf) nanocomposite. Pure gC_3N_4 shows an absorption edge at ~460 nm, whereas in the case of 95 gC_3N_4 -5BFO(exf) nanocomposite, absorption was broadened in the range of 200 to 730 nm (a broad absorption peak (highest peak intensity at 480 nm) with an absorption edge extended up to 650 nm). This result indicated that the presence of 5 wt % BFO(exf) in the 95 gC_3N_4 -5BFO(exf) nanocomposite caused enhanced visible light absorption capability of the nanocomposite compared to pure gC_3N_4 . The value of the direct band gap energy (E_g) was determined from the Tauc Plot (Figure 4f(ii)). The values E_g of BFO(exf) and pure gC_3N_4 were 2.1 and 2.9 eV respectively. The reduction of E_g in 95 gC_3N_4 -5BFO ($E_g = 2.7$ eV) compared to pure gC_3N_4 implies the existence of an electronic interaction and interfacial interaction between BFO(exf) and gC_3N_4 in the nanocomposite. In the present study, this property of the nanocomposite was exploited for the photodegradation of

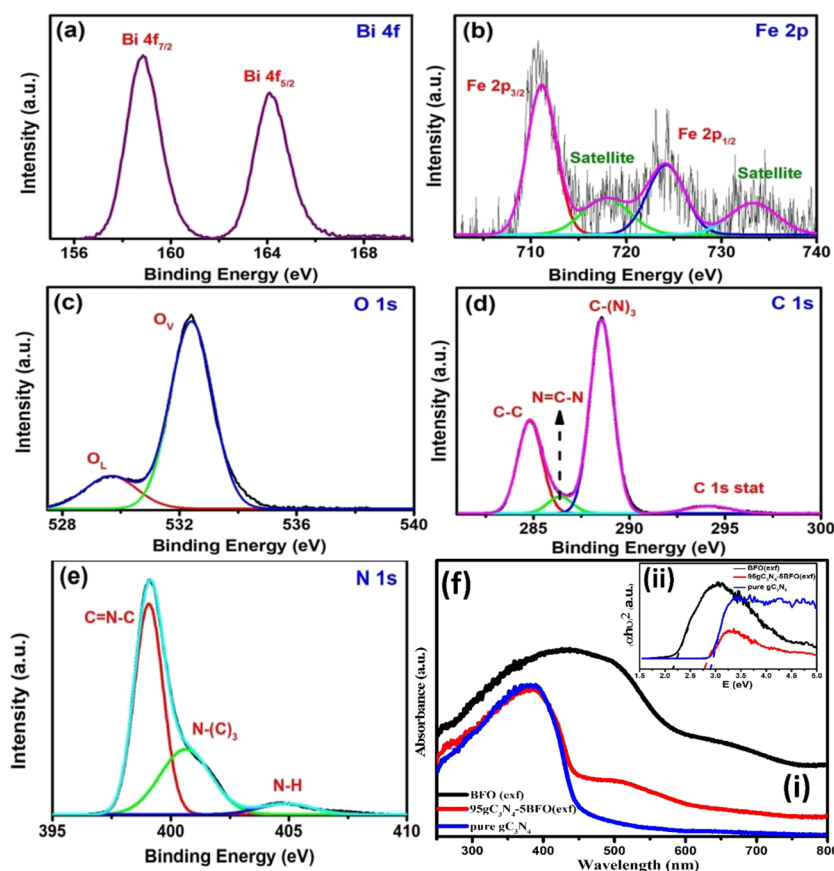
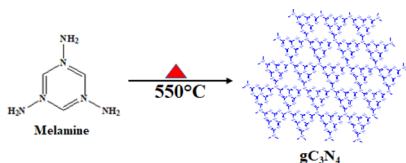


Figure 4. High-resolution XPS spectra of (a) Bi 4f, (b) Fe 2p, (c) O 1s, (d) C 1s, and (e) N 1s (f) (i) UV–vis absorption spectra and (ii) $(ah\nu)^2$ vs photon energy plots of pure gC_3N_4 , $BiFeO_3$ (exf), and $95gC_3N_4$ -5BFO(exf) nanocomposite.

Scheme 2. Formation of gC_3N_4 from Melamine



industrial dyes and antibiotics which are present as pollutants in water.

3.2. Photocatalytic Activities of the Synthesized Catalyst. To assess the photocatalytic activities of the synthesized materials, we initially performed the photodegradation of a synthetic model dye Rhodamine-B (RhB) under the exposure of a simulated solar light. Before performing the reaction, we collected the UV–vis spectra of the stock solution of RhB (0.01 mmol). Another UV–vis spectrum was collected after stirring the solution with the appropriate amount of catalyst for 30 min in the dark. It was observed that $\sim 7\%$ of RhB was adsorbed on the surface of the catalyst, which was reflected in the decrease of intensity of λ_{\max} (nm) after stirring in the dark with the catalyst compared to the initial stock solution (Figure S5a). It was observed that the intensity of λ_{\max} of RhB has been decreased, indicating the adsorption of RhB molecules on the surface of the catalyst. From this depletion of the λ_{\max} intensity, the amount of dye adsorbed in the dark by the catalyst was found to be $\sim 7\%$ in 30 min. To estimate the optimum amount of time required to establish adsorption–desorption equilibrium between the dye solution and catalyst, the same experiment was performed

again, but this time, the solution was stirred for 1 h. However, from the UV–vis spectra, it was observed that no significant increase in dye adsorption occurred due to the increase of the stirring time beyond 30 min. Hence, from now onward, we have stirred the dye solution and catalyst for 30 min dark before exposing it to the light for photocatalysis reaction.

In a typical photocatalysis reaction, the mixture of dye solution, catalyst, and H_2O_2 was exposed to the simulated solar light after the dark reaction, and we recorded UV–vis spectra periodically to monitor the percentage of photodecomposition of RhB with the progress of time. To understand the effect of the catalyst on the photodegradation reaction, we first irradiated only dye solution with simulated solar light and observed that no decomposition occurred even after 90 min of light exposure (Figure S5b). Then, we performed the reaction in the presence of H_2O_2 and synthesized materials as catalysts.

Figure 5a displays the UV–vis spectra of the photodegradation of RhB when $95gC_3N_4$ -5BFO(exf) is the catalyst. The UV–vis spectra of the photocatalysis reactions catalyzed by pure gC_3N_4 and pure BFO(exf) are presented in Figure S6. Figure 5b shows the change of the degradation amount (C_t/C_0) with the progress of time for photocatalysis reactions in the presence of different catalysts. When pure gC_3N_4 was the catalyst, we observed that ~ 210 min was required for 100% decomposition of RhB. To improve the efficiency of the catalyst, a nanocomposite having a heterojunction was prepared by combining gC_3N_4 with BFO. Pure BFO (unexfoliated) took ~ 325 min for 100% photodegradation of RhB. To improve the photocatalytic activity of BFO, we exfoliated the micrometer-size cubical structure of BFO which

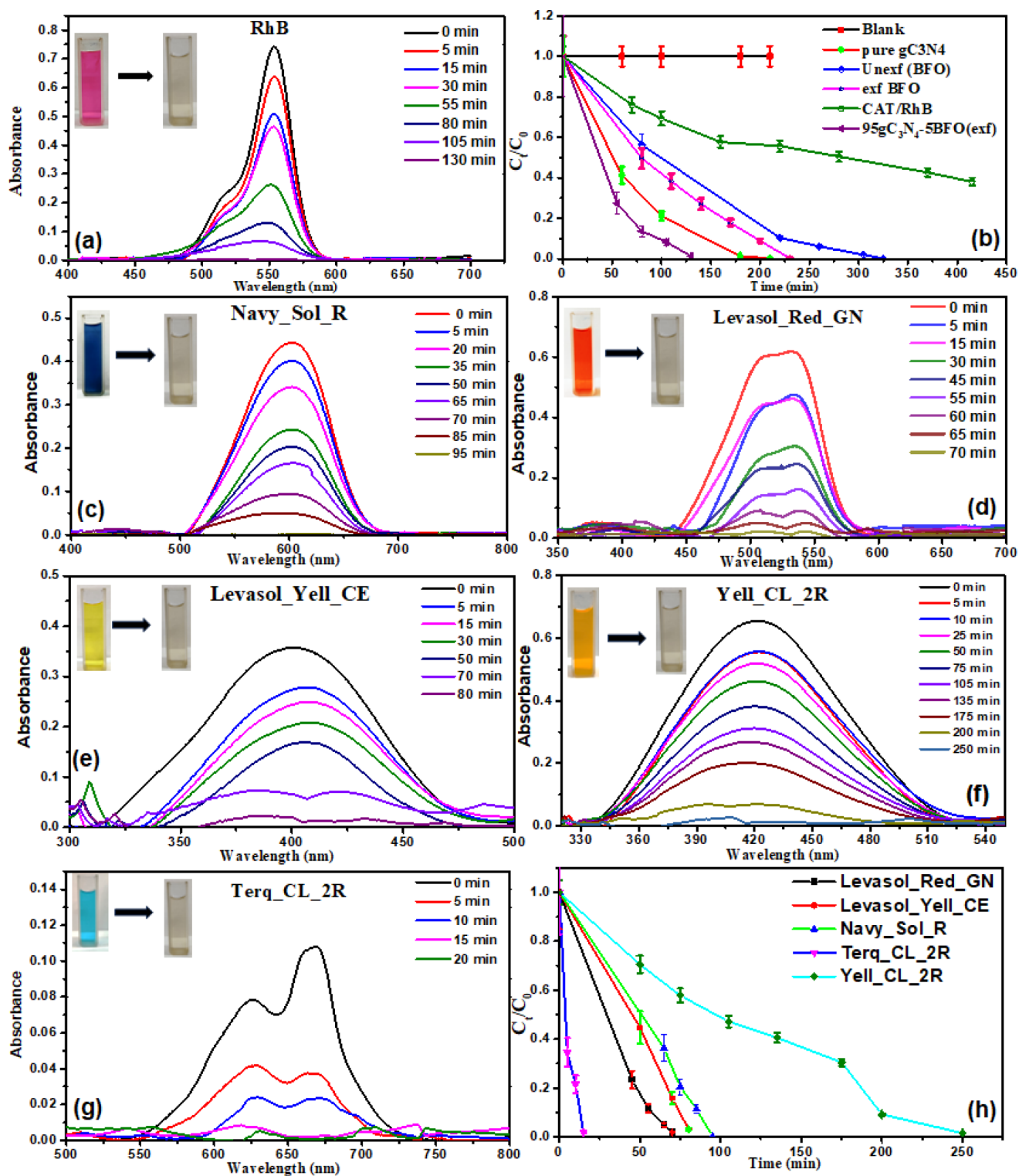


Figure 5. (a,c,d,e,f,g) Time-dependent UV-vis spectral changes of 95gC₃N₄-5BFO(exf)-catalyzed photodegradation reactions of several dyes and corresponding (b,h) C_t/C_0 vs time plot.

is composed of thin lamella to nanometer-thin flakes (BFO(exf)). We observed that the exfoliation resulted in the enhancement of the photocatalytic activity of BFO and BFO(exf) took 230 min to completely degrade RhB in the presence of H₂O₂. Observing the better efficiency of BFO(exf), we have prepared nanocomposites composed of gC₃N₄ and BFO(exf), such as 95gC₃N₄-5BFO(exf) and 90gC₃N₄-10BFO(exf).

We have observed that the presence of 5%BFO(exf) in the composition of the nanocomposite enhanced its photodegradation efficiency dramatically. A duration of 130 min was required for 100% photodegradation of RhB when 95gC₃N₄-5BFO(exf) was used as the photocatalyst in the presence of H₂O₂. However, a further increase in the BFO(exf) content caused a reduction in the catalytic efficiency of the nanocomposite. For example, the reaction completion time

was increased to ~ 185 min when photodegradation was catalyzed by $90\text{gC}_3\text{N}_4\text{-}10\text{BFO}(\text{exf})$ (Figure S6d). Hence, we have considered that the optimal composition of the catalyst is 95 wt % gC_3N_4 with 5 wt % of $\text{BFO}(\text{exf})$ (i.e., $95\text{gC}_3\text{N}_4\text{-}5\text{BFO}(\text{exf})$). The $95\text{gC}_3\text{N}_4\text{-}5\text{BFO}(\text{exf})$ catalyst reaction was also performed without H_2O_2 , and under these conditions, we have observed that $\sim 60\%$ of RhB was reduced in ~ 415 min (Figure S6e). The apparent reaction constant (k_{app}) and formal quantum efficiency (FQE) of $95\text{gC}_3\text{N}_4\text{-}5\text{BFO}(\text{exf})$ catalyzed photodegradation of RhB in the presence of H_2O_2 were $4 \times 10^{-4} \text{ s}^{-1}$ and 1.4×10^{-4} , respectively, which were greater than those parameters when the reaction was performed only with $95\text{gC}_3\text{N}_4\text{-}5\text{BFO}(\text{exf})$ and no H_2O_2 was added $k_{\text{app}} = 3.45 \times 10^{-5} \text{ s}^{-1}$ and $\text{FQE} = 1.23 \times 10^{-5}$. After the completion of the photocatalyzed degradation of RhB, the catalyst was recovered and washed thoroughly with water and ethanol. The UV–vis spectra of the solution obtained after washing showed the presence of no RhB in the washing solution. The fact indicated that $\sim 7\%$ of the dye, which was adsorbed on the catalyst surface before the photocatalysis reaction, was completely degraded during the photocatalysis reaction.

After observing the photocatalytic activity of $95\text{gC}_3\text{N}_4\text{-}5\text{BFO}(\text{exf})$ toward the degradation of a model dye Rhodamine-B, we have then tested its ability to photodegrade several commercial dyes which are used in textile industries and present in the effluents discharged from these industries. The time-dependent UV–vis spectra of the photodegradation reactions of these dyes are presented in Figure Sc–g. The extension of photodegradation of different dyes with the progress of time (C_t/C_0 vs time) is presented in Figure Sh. The time required by $95\text{gC}_3\text{N}_4\text{-}5\text{BFO}(\text{exf})$ to completely degrade these dyes as well as k_{app} and FQE values are listed in Table 1. These results demonstrate that $95\text{gC}_3\text{N}_4\text{-}5\text{BFO}(\text{exf})$ efficiently degrades commercial dyes.

Table 1. Photocatalytic Degradation of Industrial Dyes by $95\text{gC}_3\text{N}_4\text{-}5\text{BFO}(\text{exf})$

| commercial dyes | time required for 100% decomposition | k_{app} | FQE |
|-------------------|--------------------------------------|-------------------------------------|-----------------------|
| Yel CL2R | 250 min | $1 \times 10^{-4} \text{ s}^{-1}$ | 3.58×10^{-5} |
| Levasol Yellow-CE | 80 min | $4 \times 10^{-4} \text{ s}^{-1}$ | 1.43×10^{-4} |
| Levasol Red-GN | 70 min | $1.2 \times 10^{-4} \text{ s}^{-1}$ | 4.30×10^{-5} |
| Navy Sol-R | 95 min | $2 \times 10^{-4} \text{ s}^{-1}$ | 7.16×10^{-5} |
| Terq-CLSB | 15 min | $3.8 \times 10^{-4} \text{ s}^{-1}$ | 1.36×10^{-4} |

To demonstrate the ability of $95\text{gC}_3\text{N}_4\text{-}5\text{BFO}(\text{exf})$ to photodegrade different antibiotics (SMX, AMX, CPX, and SMX TCH), the photocatalysis reactions were performed, where the aqueous solutions of the antibiotics (concentrations of [TCH], [CPX], [SMX] were 10 ppm and [AMX] was 50 ppm) were irradiated by the simulated solar light in the presence of $95\text{gC}_3\text{N}_4\text{-}5\text{BFO}(\text{exf})$ intensity of λ_{max} of the antibiotic solutions (λ_{max} of SMX, AMX, CPX, and TCH were 332, 333, 330, and 372 nm respectively) was gradually diminished with the progress of the reaction and ultimately reached zero when the antibiotics were fully degraded (Figure S7).

The time required to completely degrade SMX, AMX, CPX, and TCH were 5, 5, 10, and 15 min, respectively. The photocatalytic activity of $95\text{gC}_3\text{N}_4\text{-}5\text{BFO}(\text{exf})$ was comparable and in some cases superior to the reported results (Table S1).

LCMS analysis was also performed on the antibiotic solution before and after photodegradation. The m/z values of the SMX, AMX, CPX, and TCH which were obtained before photocatalysis were 254, 365, 332, and 445, respectively. The absence of these peaks in the LCMS spectra of the antibiotic solutions after the photocatalysis reaction confirmed that the antibiotics were photodegraded. By conducting the recycling test of $95\text{gC}_3\text{N}_4\text{-}5\text{BFO}(\text{exf})$, we observed that it retained $\sim 96\%$ of its catalytic efficiency up to 5 cycles. After the reaction cycle, the catalyst was separated from the reaction mixture. The XRD pattern (Figure S8a) and microstructure (Figure S8b) were analyzed, and almost no change was observed. This fact indicates the structural robustness of the $95\text{gC}_3\text{N}_4\text{-}5\text{BFO}(\text{exf})$.

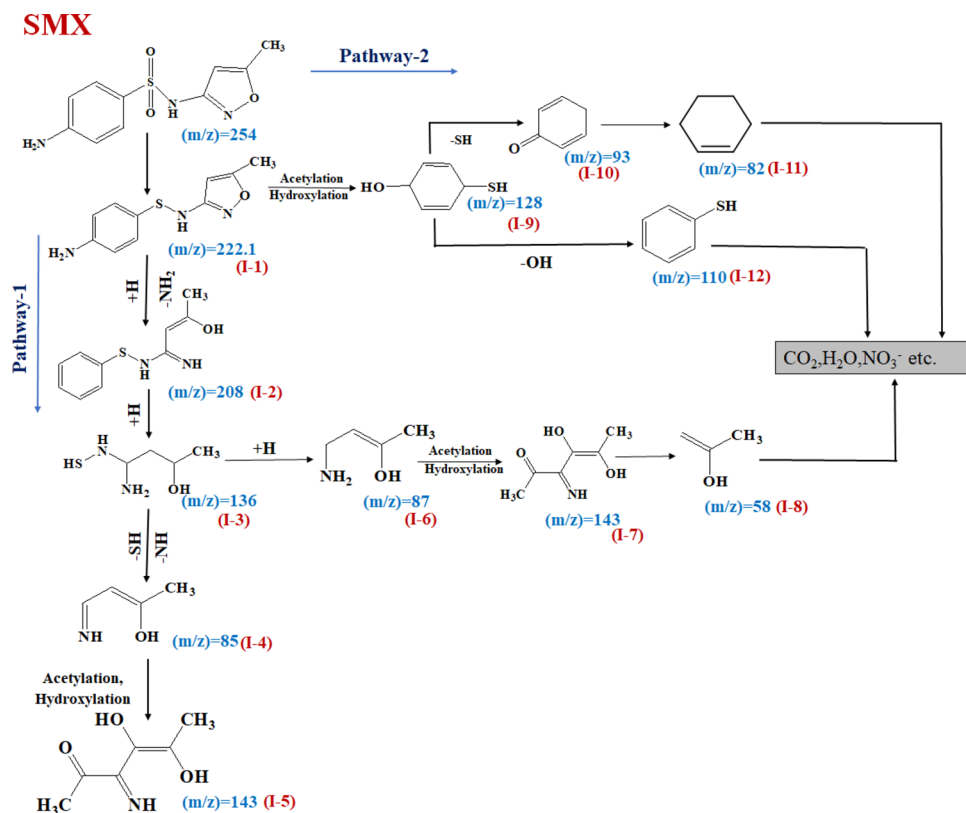
After performing the photodegradation of the antibiotics, we analyzed the fragments present in the solution by LC-MS (Figures S9–S12) and proposed the reaction pathways.

3.2.1. SMX. The results of LC-MS analysis of the reaction mixture after the degradation of SMX are discussed here. Scheme 3 illustrates the feasible degradation pathway of SMX. In pathway-1, the degradation of SMX began with the elimination of oxygen atoms of the sulfonyl group and formed I-1. Subsequently, from I-1 $-\text{NH}_2$ was lost and formed I-2. Fragmentation of I-2 led to I-3. After the elimination of a sulfonate group ($-\text{SH}$) and $-\text{NH}$ from I-3 formation of I-4 occurred. Further via acetylation and hydroxylation, I-4 produced I-5. Due to the addition, H I-4 converted to I-6. The acetylation and hydroxylation reactions of I-6 resulted in the formation of I-7, which further fragmented into I-8. To explain the formation of some of the intermediates that were detected in LC-MS spectra, a pathway (Pathway-2) was proposed which might proceed simultaneously with Pathway-1. In pathway 2, intermediate I-1 was converted to I-9. Furthermore, via the elimination of the sulfonate group, I-9 produced I-10. Reduction of I-10 formed I-11. Then by losing the $-\text{OH}$ group, I-9 decomposed to I-12. Finally, the intermediates such as (I-8, I-11, I-12) were mineralized into CO_2 , H_2O , NO_3^- , etc. Tang et al. and Li et al. have also proposed the formation of some of these intermediates during the decomposition of SMX.^{78,79}

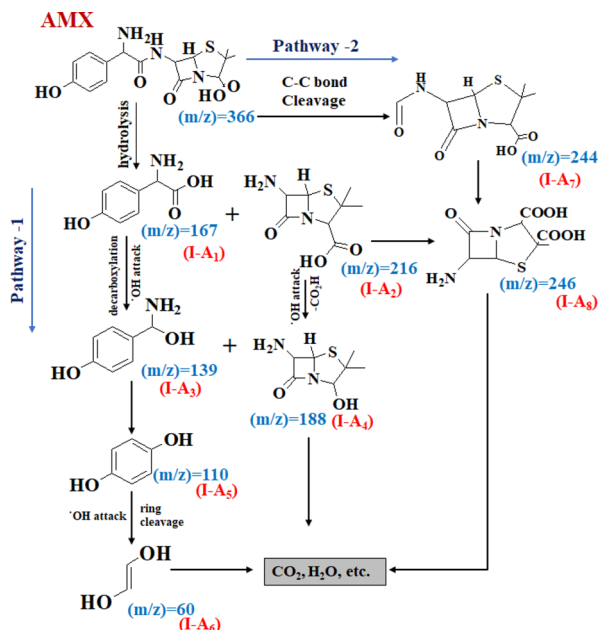
3.2.2. AMX. The plausible degradation pathway of AMX is presented in Scheme 4. In pathway 1, the hydrolysis of AMX produced I-A₁ and I-A₂. Decarboxylation of I-A₁ produced I-A₃ which further transformed to I-A₅, which then fragmented to I-A₆. Elimination of the $-\text{CO}_2\text{H}$ group by the attack of OH I-A₂ produced I-A₄. In pathway-2, I-A₇ formed from AMX via C–C bond cleavage. Oxidation of I-A₇ as well as I-A₂ led to the production of I-A₈. Finally, I-A₄, I-A₆ and I-A₈ could be mineralized to CO_2 , H_2O etc. Dou et al. and Gogoi et al. have also proposed a plausible pathway for AMX decomposition.⁸⁰

3.2.3. CPX. The plausible degradation pathway of CPX is presented in Scheme 5. In pathway 1, CPX was converted to I-B₂ via intermediate I-B₁. Cleavage of the C–N bond of I-B₂ resulted in I-B₃, which again underwent C–N bond breaking and transformed into I-B₄. Ring-opening followed by oxidation of I-B₄ produced I-B₅. The formation of I-B₅ from CPX can also be explained via pathway-2, where I-B₈ formed via the elimination of the carboxylate group from CPX. Then I-B₅ could be produced by the oxidation of I-B₈. I-B₅ can further be fragmented into small molecules such as I-B₆ followed by I-B₇. Xing et al. and Yu et al. have also proposed the formation of some of these intermediates during the decomposition of CPX.^{81–83}

Scheme 3. Plausible Mechanism of the Degradation Pathway of SMX Antibiotics based on the LC–MS Spectra



Scheme 4. Plausible Mechanism of the Degradation Pathway of AMX Antibiotics based on the LC–MS Spectra

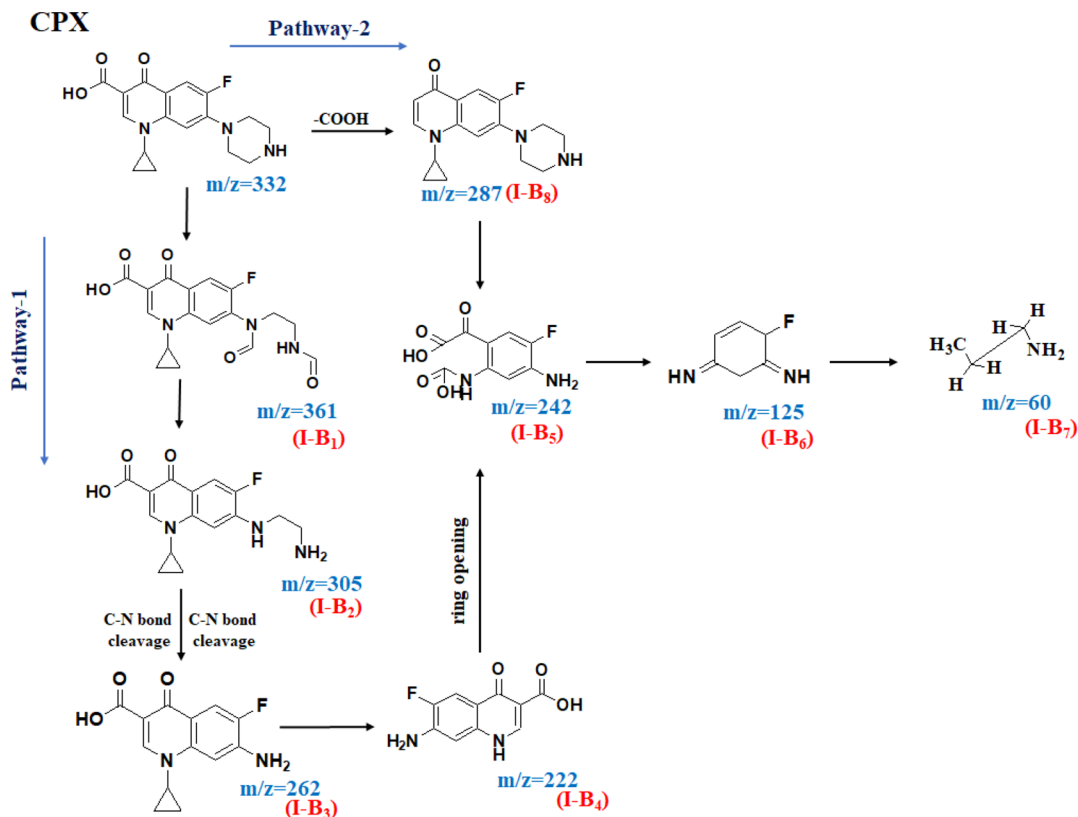


3.2.4. *TCH*. The plausible degradation pathways of *TCH* are presented in Scheme 6. The decomposition of *TCH* might proceed via Pathway 1 and Pathway 2. In pathway 1, the first hydroxylation of *TCH* produced I-C₁. N-demethylation of I-C₁ produced I-C₂. Through a deamination reaction, I-C₂ transformed into I-C₃. I-C₃ was converted into I-C₄ via deamination and ring-opening reactions. Subsequently, the dehydroxylation reactions of I-C₄ lead to the formation of I-C₅,

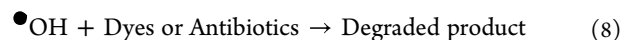
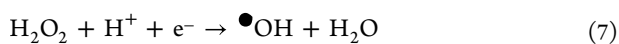
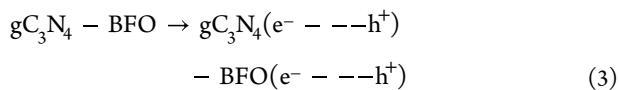
which further degraded into I-C₆ via dealkylation. I-C₆ then decomposed into I-C₇ through the loss of two hydroxyl groups. Reduction of the carbonyl group as well as elimination of –OH and –CH₃ group I-C₇ produced I-C₈. In pathway 2, the elimination of the amide group and H₂O from *TCH* resulted in the formation of I-C₁₂. *TCH* also fragmented to I-C₁₃, which produced I-C₁₄ by ring opening and breaking of the C–C bond. I-C₁₄ further disintegrated into I-C₁₅. I-C₈ was produced via the decomposition of I-C₁₂ and I-C₁₅. I-C₈ then disintegrated into small molecules such as I-C₉, I-C₁₀, and I-C₁₁. Wang et al. and Gogoi et al. have also proposed a plausible pathway for *TCH* decomposition.^{84,85}

3.2.4.1. *Plausible Reaction Mechanism Involved in the Photodegradation of Dyes and Antibiotics*. In gC₃N₄–BFO(exf) nanocomposite as gC₃N₄ is an n-type semiconductor,^{46,86,87} while BFO is a p-type semiconductor.^{88–91} In their interface, a p–n junction would be generated in the nanocomposite, and e[–] would flow spontaneously from gC₃N₄ to BFO. This process would continue until their Fermi levels (*E_f*) (*E_f* of gC₃N₄ and BFO are 0.35 and 1.39 eV, respectively) align. Pure gC₃N₄ possesses the conduction band (CB) and valence band (VB) positions at –1.13 and +1.57 eV, respectively.^{11,92,93} Whereas, pure BFO has CB and VB values of +0.31 and +2.47 eV, respectively. In this heterojunction gC₃N₄ and BFO play the role of RP and OP respectively. In the nanocomposite, when these two come in contact with each other, the electrons of gC₃N₄ infuse into BFO as a result of Coulombic attraction between them. Thus, at their contact interface, an electron depletion layer arises on gC₃N₄, and an electron accumulation layer forms on BFO. This induces the generation of an internal electric field (IEF) which assists in the recombination of photoinduced electrons in the CB of BFO and holes in the VB of gC₃N₄. Moreover, the Fermi

Scheme 5. Plausible Mechanism of the Degradation Pathway of CPX Antibiotics based on the LC–MS Spectra



energy (E_f) of BFO (1.39 eV) and gC_3N_4 (0.35 eV) aligns to the same energy level via downward and upward shifting, and in this process, bending of CB and VB occurs due to the formation of an IEF at the interface. This band bending also facilitates the transfer of photoinduced electrons in the CB of BFO downward and holes in the VB of gC_3N_4 upward, subsequently causing their recombination. On the other hand, this band bending restricts the transfer of electrons from CB (gC_3N_4) to CB (BFO) or holes from VB (BFO) to VB (gC_3N_4) in the nanocomposite. Hence, the useless photoinduced electrons and holes recombine leaving the powerful photoinduced holes in the VB of BFO and electrons in the CB of gC_3N_4 , which is the S-Scheme electron transfer Scheme 7.^{11,44–51,94,95} These powerful photogenerated holes and electrons produce hydroxyl radicals ($\bullet OH$) and superoxide radicals ($O_2^{\bullet -}$). These active radicals degrade the dye and/or antibiotic molecules to CO_2 , H_2O , and other small degradable products. The plausible reactions involved are presented in the following eqs 3–8.



To understand the role of different reactive species (such $O_2^{\bullet -}$, $\bullet OH$, H^+) on the photocatalytic degradation of RhB, we have performed the reactions in the presence of radical tapping reagents separately (e.g., parabenzoquinone (pBQ), isopropanol (IPA), 2NaEDTA) which scavenge $O_2^{\bullet -}$, $\bullet OH$, and H^+ , respectively).^{93,96–98} The photodegradation of RhB was adversely affected due to the presence of these scavengers. We observed that 52, 48, and 70% photodegradation of RhB was completed in 130 min in the presence of pBQ, IPA, and 2NaEDTA, respectively. One hundred percent photodegradation occurred within 130 min when these radical tapping agents were absent (Figure S13). The k_{app} and FQE values of these reactions are listed in Table 2. As the presence of IPA affected the reaction most, we have assumed that $\bullet OH$ plays a major role in this photocatalysis reaction. The dominant role of $\bullet OH$ in the S-Scheme pathway has also been established by several researchers by performing radical trapping experiments using different radical scavengers.^{93,96,97,99–104}

We have also recorded the photoluminescence (PL) spectra of the synthesized materials and observed that the intensity of the emission peak of gC_3N_4 is significantly higher than that of 95 gC_3N_4 -5BFO(exf) nanocomposite (Figure S14). It endorses the prevention of electron–hole recombination because of the formation of the S-Scheme heterojunction in the nanocomposite.^{95,105–107}

The aforesaid results clearly demonstrate that due to the presence of 5 wt % BFO (exf), the photocatalytic activity of 95 gC_3N_4 -5BFO(exf) significantly enhanced compared to pure gC_3N_4 . The deposition of BFO(exf) nanoflakes on and within the 2D layered structure of gC_3N_4 not only increases the

under simulated solar light irradiation. The photocatalytic activities of gC_3N_4 were enhanced significantly after decorating its surface with 5 wt % of exfoliated BFO. The enriched photodegradation performance can be attributed to the formation of S-scheme heterojunction at the interface between gC_3N_4 and BFO, where the useless photoinduced electrons and holes recombine leaving the powerful photoinduced holes in the VB of BFO and electrons in the CB of gC_3N_4 . These electrons and holes help in the formation of hydroxyl radicals ($\bullet OH$) and superoxide radicals ($O_2^{\bullet -}$), which subsequently degrade the dyes and antibiotics. The ability of this catalyst to efficiently degrade a variety of textile dyes and different types of antibiotics under simulated solar light irradiation makes it an attractive catalyst possessing enormous potential in the wastewater treatment of antibiotic- and dye-containing effluents discharged from industries.

■ ASSOCIATED CONTENT

SI Supporting Information

The Supporting Information is available free of charge at <https://pubs.acs.org/doi/10.1021/acsomega.3c05357>.

Details of chemicals; details of instruments; comparison of photocatalytic activity of $95gC_3N_4-5BFO(exf)$ with other gC_3N_4 -based photocatalysts; XRD patterns of $90gC_3N_4-10BFO(exf)$; FT-IR spectra of pure gC_3N_4 , BFO(exf) and $95gC_3N_4-5BFO(exf)$; survey spectrum of BFO- gC_3N_4 nanocomposite; UV-vis DRS spectra of pure gC_3N_4 and $95gC_3N_4-5BFO(exf)$; time-dependent UV-vis spectral changes of the photo-degradation reaction of RhB and antibiotics catalyzed by different $gC_3N_4-BFO(exf)$ nanocomposites; XRD plot and FESEM image of the used $95gC_3N_4-5BFO(exf)$ catalyst; LC-MS spectra of photo-degradation reaction of SMX, AMX, CPX, and TCH before and after degradation catalyzed by $95gC_3N_4-5BFO(exf)$; and time-dependent UV-vis spectral changes of the photodegradation reaction of RhB with radical scavengers catalyzed by $95gC_3N_4-5BFO(exf)$ and PL spectra of $95gC_3N_4-5BFO(exf)$ and BFO(exf) (PDF)

■ AUTHOR INFORMATION

Corresponding Author

Narendra Nath Ghosh – Nano-Materials Lab, Department of Chemistry, Birla Institute of Technology and Science, Sancoale, Goa 403726, India; orcid.org/0000-0002-8338-7292; Email: naren70@yahoo.com; Fax: +91 832 2580318/25570339

Authors

Darshana Anand Upar – Nano-Materials Lab, Department of Chemistry, Birla Institute of Technology and Science, Sancoale, Goa 403726, India

Debika Gogoi – Nano-Materials Lab, Department of Chemistry, Birla Institute of Technology and Science, Sancoale, Goa 403726, India

Manash R. Das – Advanced Materials Group, Materials Sciences and Technology Division, CSIR-NEIST, Jorhat, Assam 785006, India; Academy of Scientific and Innovative Research (AcSIR), Ghaziabad 201002, India; orcid.org/0000-0002-6317-7933

Bhanudas Naik – DCTs Dhempe College of Arts & Science, Miramar, Goa 403001, India

Complete contact information is available at: <https://pubs.acs.org/10.1021/acsomega.3c05357>

Notes

The authors declare no competing financial interest.

■ ACKNOWLEDGMENTS

We are thankful to Vasantrao Dempo Education and Research Foundation for providing financial support for the project. Use of the equipment of the Central Sophisticated Instrumentation Facility (CSIF) of BITS Pilani, K K Birla Goa Campus (FESEM, EDX elemental mapping, and Raman Spectroscopy) is acknowledged. Also, the authors are thankful to CSIR-North East Institute of Science and Technology, Jorhat, for the facility of XPS analysis.

■ REFERENCES

- (1) Garrick, D.; Hall, J. W. Water security and society: risks, metrics, and pathways. *Annu. Rev. Env. Resour.* **2014**, *39*, 611–639.
- (2) Rocha, J.; Oliveira, S.; Viana, C. M.; Ribeiro, A. I. Climate change and its impacts on health, environment and economy. In *One Health*; Elsevier, 2022; pp 253–279.
- (3) du Plessis, A. Persistent degradation: Global water quality challenges and required actions. *One Earth* **2022**, *5* (2), 129–131.
- (4) Gu, D.; Pelletier, F.; Sawyer, C. *Projecting Age-sex-specific Mortality: A Comparison of the Modified Lee-Carter and Pattern of Mortality Decline Methods*; Technical Paper No. 6; UN Population Division; United Nations: New York, 2017,2.
- (5) Melchionna, M.; Fornasiero, P. Updates on the Roadmap for Photocatalysis. *ACS Catal.* **2020**, *10* (10), 5493–5501.
- (6) Khan, S. B.; Khan, M. S. J.; Akhtar, K.; Bakhsh, E. M.; Kamal, T.; Asiri, A. M.; Shen, Y. Design of efficient solar photocatalytic system for hydrogen production and degradation of environmental pollutant. *J. Mater. Res. Technol.* **2021**, *14*, 2497–2512.
- (7) Ghosh, B. K.; Ghosh, N. N. Applications of metal nanoparticles as catalysts in cleaning dyes containing industrial effluents: a review. *J. Nanosci. Nanotechnol.* **2018**, *18* (6), 3735–3758.
- (8) Sarkar, S.; Banerjee, A.; Halder, U.; Biswas, R.; Bandopadhyay, R. Degradation of synthetic azo dyes of textile industry: a sustainable approach using microbial enzymes. *Water Sci. Eng.* **2017**, *2*, 121–131.
- (9) Baban, A.; Yediler, A.; Lienert, D.; Kemerdere, N.; Kettrup, A. Ozonation of high strength segregated effluents from a woollen textile dyeing and finishing plant. *Dyes Pigment.* **2003**, *58* (2), 93–98.
- (10) Patel, R.; Suresh, S. Decolourization of azo dyes using magnesium–palladium system. *J. Hazard. Mater.* **2006**, *137* (3), 1729–1741.
- (11) Gogoi, D.; Makkar, P.; Ghosh, N. N. Solar light-irradiated photocatalytic degradation of model dyes and industrial dyes by a magnetic $CoFe_2O_4-gC_3N_4$ S-scheme heterojunction photocatalyst. *ACS Omega* **2021**, *6* (7), 4831–4841.
- (12) Shao, Y.; Wang, Y.; Yuan, Y.; Xie, Y. A systematic review on antibiotics misuse in livestock and aquaculture and regulation implications in China. *Sci. Total Environ.* **2021**, 798, No. 149205.
- (13) Anee, I. J.; Alam, S.; Begum, R. A.; Shahjahan, R. M.; Khandaker, A. M. The role of probiotics on animal health and nutrition. *J. Basic Appl. Zool.* **2021**, *82*, 1–16.
- (14) Liu, Y.; Yan, T.; Li, X.; Duan, Y.; Yang, X.; Yang, X. Effects of *Bacillus subtilis* and antibiotic growth promoters on the growth performance, intestinal function and gut microbiota of pullets from 0 to 6 weeks. *Animal* **2020**, *14* (8), 1619–1628.
- (15) Xin, S.; Liu, G.; Ma, X.; Gong, J.; Ma, B.; Yan, Q.; Chen, Q.; Ma, D.; Zhang, G.; Gao, M. High efficiency heterogeneous Fenton-like catalyst biochar modified $CuFeO_2$ for the degradation of tetracycline: economical synthesis, catalytic performance and mechanism. *Appl. Catal., B* **2021**, *280*, No. 119386.

- (16) Ray, S. K.; Dhakal, D.; Lee, S. W. Insight into sulfamethoxazole degradation, mechanism, and pathways by AgBr-BaMoO₄ composite photocatalyst. *J. Photochem. Photobiol. A* **2018**, *364*, 686–695.
- (17) Hanna, N.; Sun, P.; Sun, Q.; Li, X.; Yang, X.; Ji, X.; Zou, H.; Ottoson, J.; Nilsson, L. E.; Berglund, B. Presence of antibiotic residues in various environmental compartments of Shandong province in eastern China: its potential for resistance development and ecological and human risk. *Environ. Int.* **2018**, *114*, 131–142.
- (18) Polianciuc, S. I.; Gurzău, A. E.; Kiss, B.; Ștefan, M. G.; Loghin, F. Antibiotics in the environment: causes and consequences. *Med. Pharm. Rep.* **2015**, *93* (3), 231.
- (19) Gogoi, D.; Karmur, R. S.; Das, M. R.; Ghosh, N. N. Cu and CoFe₂O₄ nanoparticles decorated hierarchical porous carbon: An excellent catalyst for reduction of nitroaromatics and microwave-assisted antibiotic degradation. *Appl. Catal., B* **2022**, *312*, No. 121407.
- (20) Salimi, M.; Behbahani, M.; Sobhi, H. R.; Gholami, M.; Jafari, A. J.; Kalantary, R. R.; Farzadkia, M.; Esrafil, A. A new nano-photocatalyst based on Pt and Bi co-doped TiO₂ for efficient visible-light photo degradation of amoxicillin. *New J. Chem.* **2019**, *43* (3), 1562–1568.
- (21) Bafana, A.; Devi, S. S.; Chakrabarti, T. Azo dyes: past, present and the future. *Environ. Rev.* **2011**, *19*, 350–371.
- (22) Ahmad, A.; Mohd-Setapar, S. H.; Chuong, C. S.; Khatoon, A.; Wani, W. A.; Kumar, R.; Rafatullah, M. Recent advances in new generation dye removal technologies: novel search for approaches to reprocess wastewater. *RSC Adv.* **2015**, *5* (39), 30801–30818.
- (23) Divyapriya, G.; Nambi, I. M.; Senthilnathan, J. Nanocatalysts in Fenton based advanced oxidation process for water and wastewater treatment. *J. Bionanosci.* **2016**, *10* (5), 356–368.
- (24) Gupta, V. Application of low-cost adsorbents for dye removal—a review. *J. Environ. Manage.* **2009**, *90* (8), 2313–2342.
- (25) Verma, A. K.; Dash, R. R.; Bhunia, P. A review on chemical coagulation/flocculation technologies for removal of colour from textile wastewaters. *J. Environ. Manage.* **2012**, *93* (1), 154–168.
- (26) Oturan, M. A.; Aaron, J.-J. Advanced oxidation processes in water/wastewater treatment: principles and applications. A review. *Crit. Rev. Environ. Sci. Technol.* **2014**, *44* (23), 2577–2641.
- (27) Asghar, A.; Raman, A. A. A.; Daud, W. M. A. W. Advanced oxidation processes for in-situ production of hydrogen peroxide/hydroxyl radical for textile wastewater treatment: a review. *J. Clean. Prod.* **2015**, *87*, 826–838.
- (28) Robinson, T.; McMullan, G.; Marchant, R.; Nigam, P. Remediation of dyes in textile effluent: a critical review on current treatment technologies with a proposed alternative. *Bioresour. Technol.* **2001**, *77* (3), 247–255.
- (29) Slokar, Y. M.; Le Marechal, A. M. Methods of decoloration of textile wastewaters. *Dyes Pigm.* **1998**, *37* (4), 335–356.
- (30) Schneider, J.; Matsuoka, M.; Takeuchi, M.; Zhang, J.; Horiuchi, Y.; Anpo, M.; Bahnemann, D. W. Understanding TiO₂ photocatalysis: mechanisms and materials. *Chem. Rev.* **2014**, *114* (19), 9919–9986.
- (31) Lee, K. M.; Lai, C. W.; Ngai, K. S.; Juan, J. C. Recent developments of zinc oxide based photocatalyst in water treatment technology: a review. *Water Res.* **2016**, *88*, 428–448.
- (32) Kumar, S. G.; Devi, L. G. Review on modified TiO₂ photocatalysis under UV/visible light: selected results and related mechanisms on interfacial charge carrier transfer dynamics. *J. Phys. Chem. A* **2011**, *115* (46), 13211–13241.
- (33) Nakata, K.; Fujishima, A. TiO₂ photocatalysis: Design and applications. *J. Photochem. Photobiol., C* **2012**, *13* (3), 169–189.
- (34) Fujishima, A.; Rao, T. N.; Tryk, D. A. Titanium dioxide photocatalysis. *J. Photochem. Photobiol., C* **2000**, *1* (1), 1–21.
- (35) Fujishima, A.; Zhang, X. Titanium dioxide photocatalysis: present situation and future approaches. *C. R. Chim.* **2006**, *9* (5–6), 750–760.
- (36) Zhang, F.; Li, Y.-H.; Li, J.-Y.; Tang, Z.-R.; Xu, Y.-J. 3D graphene-based gel photocatalysts for environmental pollutants degradation. *Environ. Pollut.* **2019**, *253*, 365–376.
- (37) Weng, B.; Lu, K.-Q.; Tang, Z.; Chen, H. M.; Xu, Y.-J. Stabilizing ultrasmall Au clusters for enhanced photoredox catalysis. *Nat. Commun.* **2018**, *9* (1), 1543.
- (38) Li, Y.-H.; Li, J.-Y.; Xu, Y.-J. Bimetallic nanoparticles as cocatalysts for versatile photoredox catalysis. *Energy Chem.* **2021**, *3* (1), No. 100047.
- (39) Zhang, N.; Yang, M.-Q.; Liu, S.; Sun, Y.; Xu, Y.-J. Waltzing with the versatile platform of graphene to synthesize composite photocatalysts. *Chem. Rev.* **2015**, *115* (18), 10307–10377.
- (40) Han, C.; Li, Y.-H.; Qi, M.-Y.; Zhang, F.; Tang, Z.-R.; Xu, Y.-J. Surface/Interface Engineering of Carbon-Based Materials for Constructing Multidimensional Functional Hybrids. *Sol. RRL* **2020**, *4* (8), No. 1900577.
- (41) Low, J.; Yu, J.; Jaroniec, M.; Wageh, S.; Al-Ghamdi, A. A. Heterojunction photocatalysts. *Adv. Mater.* **2017**, *29* (20), No. 1601694.
- (42) Murugesan, P.; Moses, J.; Anandharamkrishnan, C. Photocatalytic disinfection efficiency of 2D structure graphitic carbon nitride-based nanocomposites: a review. *J. Mater. Sci.* **2019**, *54* (19), 12206–12235.
- (43) Wen, J.; Xie, J.; Chen, X.; Li, X. A review on g-C₃N₄-based photocatalysts. *Appl. Surf. Sci.* **2017**, *391*, 72–123.
- (44) Fu, J.; Xu, Q.; Low, J.; Jiang, C.; Yu, J. Ultrathin 2D/2D WO₃/g-C₃N₄ step-scheme H₂-production photocatalyst. *Appl. Catal., B* **2019**, *243*, 556–565.
- (45) Xu, Q.; Zhang, L.; Cheng, B.; Fan, J.; Yu, J. S-scheme heterojunction photocatalyst. *Chem* **2020**, *6* (7), 1543–1559.
- (46) Tran Huu, H.; Thi, M. D. N.; Nguyen, V. P.; Thi, L. N.; Phan, T. T. T.; Hoang, Q. D.; Luc, H. H.; Kim, S. J.; Vo, V. One-pot synthesis of S-scheme MoS₂/g-C₃N₄ heterojunction as effective visible light photocatalyst. *Sci. Rep.* **2021**, *11* (1), 14787.
- (47) Dong, Z.; Zhou, J.; Zhang, Z.; Jiang, Y.; Zhou, R.; Yao, C. Construction of a p–n Type S-Scheme Heterojunction by Incorporating CsPbBr₃ Nanocrystals into Mesoporous Cu₂O Microspheres for Efficient CO₂ Photoreduction. *ACS Appl. Energy Mater.* **2022**, *5* (8), 10076–10085.
- (48) Han, X.; Lu, B.; Huang, X.; Liu, C.; Chen, S.; Chen, J.; Zeng, Z.; Deng, S.; Wang, J. Novel p-and n-type S-scheme heterojunction photocatalyst for boosted CO₂ photoreduction activity. *Appl. Catal., B* **2022**, *316*, No. 121587.
- (49) Wang, X.; Sayed, M.; Ruzimuradov, O.; Zhang, J.; Fan, Y.; Li, X.; Bai, X.; Low, J. A review of step-scheme photocatalysts. *Appl. Mater. Today* **2022**, *29*, No. 101609.
- (50) Xu, Q.; Wageh, S.; Al-Ghamdi, A. A.; Li, X. Design principle of S-scheme heterojunction photocatalyst. *J. Mater. Sci. Technol.* **2022**, *124*, 171–173.
- (51) Bao, Y.; Song, S.; Yao, G.; Jiang, S. S-scheme photocatalytic systems. *Sol. RRL* **2021**, *5* (7), No. 2100118.
- (52) Ikram, M.; Rashid, M.; Haider, A.; Naz, S.; Haider, J.; Raza, A.; Ansar, M.; Uddin, M. K.; Ali, N. M.; Ahmed, S. S. A review of photocatalytic characterization, and environmental cleaning, of metal oxide nanostructured materials. *SM&T* **2021**, *30*, No. e00343.
- (53) Ren, G.; Han, H.; Wang, Y.; Liu, S.; Zhao, J.; Meng, X.; Li, Z. Recent advances of photocatalytic application in water treatment: A review. *Nanomater.* **2021**, *11* (7), 1804.
- (54) Xu, Y.-J. Promises and challenges in photocatalysis. *Frontiers Media SA* **2021**, *1*, No. 708319.
- (55) Twilton, J.; Le, C.; Zhang, P.; Shaw, M. H.; Evans, R. W.; MacMillan, D. W. The merger of transition metal and photocatalysis. *Nat. Rev. Chem.* **2017**, *1* (7), No. 0052.
- (56) Dong, S.; Feng, J.; Fan, M.; Pi, Y.; Hu, L.; Han, X.; Liu, M.; Sun, J.; Sun, J. Recent developments in heterogeneous photocatalytic water treatment using visible light-responsive photocatalysts: a review. *RSC Adv.* **2015**, *5* (19), 14610–14630.
- (57) Dharma, H. N. C.; Jaafar, J.; Widiastuti, N.; Matsuyama, H.; Rajabsadeh, S.; Othman, M. H. D.; Rahman, M. A.; Jafri, N. N. M.; Suhaimin, N. S.; Nasir, A. M. A review of titanium dioxide (TiO₂)-based photocatalyst for oilfield-produced water treatment. *Membranes* **2022**, *12* (3), 345.

- (58) Fan, Q.; Huang, Y.; Zhang, C.; Liu, J.; Piao, L.; Yu, Y.; Zuo, S.; Li, B. Superior nanoporous graphitic carbon nitride photocatalyst coupled with CdS quantum dots for photodegradation of RhB. *Catal. Today* **2016**, *264*, 250–256.
- (59) Pawar, R. C.; Khare, V.; Lee, C. S. Hybrid photocatalysts using graphitic carbon nitride/cadmium sulfide/reduced graphene oxide (g-C₃N₄/CdS/RGO) for superior photodegradation of organic pollutants under UV and visible light. *Dalton Trans.* **2014**, *43* (33), 12514–12527.
- (60) Alcudia-Ramos, M.; Fuentes-Torres, M.; Ortiz-Chi, F.; Espinosa-González, C.; Hernández-Como, N.; García-Zaleta, D.; Kesarla, M.; Torres-Torres, J.; Collins-Martínez, V.; Godavarthi, S. Fabrication of g-C₃N₄/TiO₂ heterojunction composite for enhanced photocatalytic hydrogen production. *Ceram. Int.* **2020**, *46* (1), 38–45.
- (61) Rhaman, M.; Matin, M.; Hossain, M.; Mozahid, F.; Hakim, M.; Islam, M. Bandgap engineering of cobalt-doped bismuth ferrite nanoparticles for photovoltaic applications. *Bull. Mater. Sci.* **2019**, *42* (4), 190.
- (62) Shen, H.; Zhao, X.; Duan, L.; Liu, R.; Li, H. Enhanced visible light photocatalytic activity in SnO₂@g-C₃N₄ core-shell structures. *Mater. Sci. Eng., B* **2017**, *218*, 23–30.
- (63) Dong, F.; Sun, Y.; Wu, L.; Fu, M.; Wu, Z. Facile transformation of low cost thiourea into nitrogen-rich graphitic carbon nitride nanocatalyst with high visible light photocatalytic performance. *Catal. Sci. Technol.* **2012**, *2* (7), 1332–1335.
- (64) Hu, S.; Ma, L.; You, J.; Li, F.; Fan, Z.; Lu, G.; Liu, D.; Gui, J. Enhanced visible light photocatalytic performance of g-C₃N₄ photocatalysts co-doped with iron and phosphorus. *Appl. Surf. Sci.* **2014**, *311*, 164–171.
- (65) Moitra, D.; Dhole, S.; Ghosh, B. K.; Chandel, M.; Jani, R. K.; Patra, M. K.; Vadera, S. R.; Ghosh, N. N. Synthesis and microwave absorption properties of BiFeO₃ nanowire-RGO nanocomposite and first-principles calculations for insight of electromagnetic properties and electronic structures. *J. Phys. Chem. C* **2017**, *121* (39), 21290–21304.
- (66) Wang, H.; Zhang, X.; Xie, J.; Zhang, J.; Ma, P.; Pan, B.; Xie, Y. Structural distortion in graphitic-C₃N₄ realizing an efficient photoreactivity. *Nanoscale* **2015**, *7* (12), 5152–5156.
- (67) Shiraiishi, Y.; Kanazawa, S.; Sugano, Y.; Tsukamoto, D.; Sakamoto, H.; Ichikawa, S.; Hirai, T. Highly selective production of hydrogen peroxide on graphitic carbon nitride (g-C₃N₄) photocatalyst activated by visible light. *ACS Catal.* **2014**, *4* (3), 774–780.
- (68) Xiang, Q.; Yu, J.; Jaroniec, M. Preparation and enhanced visible-light photocatalytic H₂-production activity of graphene/C₃N₄ composites. *J. Phys. Chem. C* **2011**, *115* (15), 7355–7363.
- (69) Moitra, D.; Ghosh, B. K.; Chandel, M.; Ghosh, N. N. Synthesis of a BiFeO₃ nanowire-reduced graphene oxide based magnetically separable nanocatalyst and its versatile catalytic activity towards multiple organic reactions. *RSC Adv.* **2016**, *6* (100), 97941–97952.
- (70) Eledath, M.; Chandran, M. Raman study of BiFeO₃ nanostructures using different excitation wavelengths: Effects of crystallite size on vibrational modes. *J. Phys. Chem. Solids* **2023**, *172*, No. 111060.
- (71) Ye, L.; Liu, J.; Gong, C.; Tian, L.; Peng, T.; Zan, L. Two different roles of metallic Ag on Ag/AgX/BiOX (X= Cl, Br) visible light photocatalysts: surface plasmon resonance and Z-scheme bridge. *ACS Catal.* **2012**, *2* (8), 1677–1683.
- (72) Di, L.; Yang, H.; Xian, T.; Chen, X. Enhanced photocatalytic activity of NaBH₄ reduced BiFeO₃ nanoparticles for rhodamine B decolorization. *Mater.* **2017**, *10* (10), 1118.
- (73) Reddy, B. P.; Rajendar, V.; Shekar, M.; Park, S. Particle Size Effects on the Photocatalytic Activity of BiFeO₃ particles. *Dig. J. Nanomater. Biostructures* **2018**, *13* (1), 87–95.
- (74) Wang, K.; Li, J.; Zhang, G. Ag-bridged Z-scheme 2D/2D Bi₂FeTi₃O₁₅/g-C₃N₄ heterojunction for enhanced photocatalysis: mediator-induced interfacial charge transfer and mechanism insights. *ACS Appl. Mater. Interfaces* **2019**, *11* (31), 27686–27696.
- (75) Wang, J.; Tang, L.; Zeng, G.; Liu, Y.; Zhou, Y.; Deng, Y.; Wang, J.; Peng, B. Plasmonic Bi metal deposition and g-C₃N₄ coating on Bi₂WO₆ microspheres for efficient visible-light photocatalysis. *ACS Sustain. Chem. Eng.* **2017**, *5* (1), 1062–1072.
- (76) Vu, N.-N.; Kaliaguine, S.; Do, T.-O. Synthesis of the g-C₃N₄/CdS nanocomposite with a chemically bonded interface for enhanced sunlight-driven CO₂ photoreduction. *ACS Appl. Energy Mater.* **2020**, *3* (7), 6422–6433.
- (77) Gholipour, M. R.; Béland, F.; Do, T.-O. Post-calcined carbon nitride nanosheets as an efficient photocatalyst for hydrogen production under visible light irradiation. *ACS Sustain. Chem. Eng.* **2017**, *5* (1), 213–220.
- (78) Tang, T.; Liu, M.; Chen, Y.; Du, Y.; Feng, J.; Feng, H. Influence of sulfamethoxazole on anaerobic digestion: Methanogenesis, degradation mechanism and toxicity evolution. *J. Hazard. Mater.* **2022**, *431*, No. 128540.
- (79) Li, Y.; He, J.; Zhang, K.; Hong, P.; Wang, C.; Kong, L.; Liu, J. Oxidative degradation of sulfamethoxazole antibiotic catalyzed by porous magnetic manganese ferrite nanoparticles: mechanism and by-products identification. *J. Mater. Sci.* **2020**, *55*, 13767–13784.
- (80) Dou, M.; Wang, J.; Gao, B.; Xu, C.; Yang, F. Photocatalytic difference of amoxicillin and cefotaxime under visible light by mesoporous g-C₃N₄: mechanism, degradation pathway and DFT calculation. *J. Chem. Eng.* **2020**, *383*, No. 123134.
- (81) Xing, S.; Li, T.; Gao, Y.; Liu, J. Insight into the mechanism for photocatalytic degradation of ciprofloxacin with CeO₂. *Optik* **2019**, *183*, 266–272.
- (82) Yu, X.; Zhang, J.; Zhang, J.; Niu, J.; Zhao, J.; Wei, Y.; Yao, B. Photocatalytic degradation of ciprofloxacin using Zn-doped Cu₂O particles: analysis of degradation pathways and intermediates. *J. Chem. Eng.* **2019**, *374*, 316–327.
- (83) Sarafraz, M.; Sadeghi, M.; Yazdanbakhsh, A.; Amini, M. M.; Sadani, M.; Eslami, A. Enhanced photocatalytic degradation of ciprofloxacin by black Ti₃+N-TiO₂ under visible LED light irradiation: Kinetic, energy consumption, degradation pathway, and toxicity assessment. *Process Saf. Environ. Prot.* **2020**, *137*, 261–272.
- (84) Wang, Q.; Li, P.; Zhang, Z.; Jiang, C.; Zuoqiao, K.; Liu, J.; Wang, Y. Kinetics and mechanism insights into the photodegradation of tetracycline hydrochloride and ofloxacin mixed antibiotics with the flower-like BiOCl/TiO₂ heterojunction. *J. Photochem. Photobiol., A* **2019**, *378*, 114–124.
- (85) Wang, C.; Cai, M.; Liu, Y.; Yang, F.; Zhang, H.; Liu, J.; Li, S. Facile construction of novel organic–inorganic tetra (4-carboxyphenyl) porphyrin/Bi₂MoO₆ heterojunction for tetracycline degradation: Performance, degradation pathways, intermediate toxicity analysis and mechanism insight. *J. Colloid Interface Sci.* **2022**, *605*, 727–740.
- (86) Jiang, J.; Song, Y.; Wang, X.; Li, T.; Li, M.; Lin, Y.; Xie, T.; Dong, S. Enhancing aqueous pollutant photodegradation via a Fermi level matched Z-scheme BiOI/Pt/g-C₃N₄ photocatalyst: unobstructed photogenerated charge behavior and degradation pathway exploration. *Catal. Sci. Technol.* **2020**, *10* (10), 3324–3333.
- (87) Jing, J.; Chen, Z.; Feng, C.; Sun, M.; Hou, J. Transforming g-C₃N₄ from amphoteric to n-type semiconductor: The important role of p/n type on photoelectrochemical cathodic protection. *J. Alloys Compd.* **2021**, *851*, No. 156820.
- (88) Yang, H.; Luo, H.; Wang, H.; Usov, I.; Suvorova, N.; Jain, M.; Feldmann, D.; Dowden, P.; DePaula, R.; Jia, Q. Rectifying current-voltage characteristics of BiFeO₃/Nb-doped SrTiO₃ heterojunction. *Appl. Phys. Lett.* **2008**, *92* (10), No. 2896302.
- (89) Xu, Q.; Sobhan, M.; Yang, Q.; Anariba, F.; Ong, K. P.; Wu, P. The role of Bi vacancies in the electrical conduction of BiFeO₃: a first-principles approach. *Dalton Trans.* **2014**, *43* (28), 10787–10793.
- (90) Zhao, L.; Lu, Z.; Zhang, F.; Tian, G.; Song, X.; Li, Z.; Huang, K.; Zhang, Z.; Qin, M.; Sujuan, W. Current rectifying and resistive switching in high density BiFeO₃ nanocapacitor arrays on Nb-SrTiO₃ substrates. *Sci. Rep.* **2015**, *5* (1), 9680.
- (91) Nkwachukwu, O. V.; Muzenda, C.; Jayeola, K. D.; Sebokolodi, T. I.; Sipuka, D. S.; Wu, H.; Koiki, B. A.; Zhou, M.; Arotiba, O. A. Characterisation and application of bismuth ferrite-bismuth vanadate pn heterojunction in the photoelectrocatalytic degradation of ciprofloxacin in water. *Electrochim. Acta* **2023**, *454*, No. 142385.

- (92) Ge, L.; Han, C.; Liu, J. In situ synthesis and enhanced visible light photocatalytic activities of novel PANI-gC₃N₄ composite photocatalysts. *J. Mater. Chem.* **2012**, *22* (23), 11843–11850.
- (93) Huang, S.; Xu, Y.; Xie, M.; Xu, H.; He, M.; Xia, J.; Huang, L.; Li, H. Synthesis of magnetic CoFe₂O₄/g-C₃N₄ composite and its enhancement of photocatalytic ability under visible-light. *Colloids Surf., A* **2015**, *478*, 71–80.
- (94) Gogoi, D.; Das, M. R.; Ghosh, N. N. 2-D gC₃N₄ supported CoFe₂O₄ nanoparticles as an efficient S-scheme catalyst for various antibiotic degradation. *Appl. Surf. Sci.* **2023**, *619*, No. 156753.
- (95) Gogoi, D.; Makkar, P.; Korde, R.; Das, M. R.; Ghosh, N. N. Exfoliated gC₃N₄ supported CdS nanorods as a S-scheme heterojunction photocatalyst for the degradation of various textile dyes. *Adv. Powder Technol.* **2022**, *33* (11), No. 103801.
- (96) Tian, Y.; Chang, B.; Lu, J.; Fu, J.; Xi, F.; Dong, X. Hydrothermal synthesis of graphitic carbon nitride–Bi₂WO₆ heterojunctions with enhanced visible light photocatalytic activities. *ACS Appl. Mater. Interfaces* **2013**, *5* (15), 7079–7085.
- (97) Yao, Y.; Cai, Y.; Lu, F.; Qin, J.; Wei, F.; Xu, C.; Wang, S. Magnetic ZnFe₂O₄-C₃N₄ hybrid for photocatalytic degradation of aqueous organic pollutants by visible light. *Ind. Eng. Chem. Res.* **2014**, *53* (44), 17294–17302.
- (98) Guo, X.; Ai, S.; Yang, D.; Zhao, L.; Ding, H. Synergistic photocatalytic and Fenton-like degradation of organic contaminants using peroxymonosulfate activated by CoFe₂O₄@ g-C₃N₄ composite. *Environ. Technol.* **2021**, *42* (14), 2240–2253.
- (99) Abd-Rabboh, H. S.; Galal, A.; Aziz, R. A.; Ahmed, M. A novel BiVO₃/SnO₂ step S-scheme nano-heterojunction for an enhanced visible light photocatalytic degradation of amaranth dye and hydrogen production. *RSC Adv.* **2021**, *11* (47), 29507–29518.
- (100) Xie, Q.; He, W.; Liu, S.; Li, C.; Zhang, J.; Wong, P. K. Bifunctional S-scheme g-C₃N₄/Bi/BiVO₄ hybrid photocatalysts toward artificial carbon cycling. *Chin. J. Catal.* **2020**, *41* (1), 140–153.
- (101) Kumar, Y.; Sudhaik, A.; Sharma, K.; Raizada, P.; Khan, A. A. P.; Nguyen, V.-H.; Ahamad, T.; Singh, P.; Asiri, A. M. Construction of magnetically separable novel arrow down dual S-scheme ZnIn₂S₄/BiOCl/FeVO₄ heterojunction for improved photocatalytic activity. *J. Photochem. Photobiol., A* **2023**, *435*, No. 114326.
- (102) Li, Y.; Zhang, H.; Qian, W.; Xia, Y.; Li, D.; Guo, Z. Construction of S-scheme heterostructured TiO₂/g-C₃N₄ composite microspheres with sunlight-driven photocatalytic activity. *Mater. Today Commun.* **2023**, *36*, No. 106431.
- (103) Xian, T.; Yang, H.; Di, L.; Dai, J. Enhanced photocatalytic activity of BaTiO₃@g-C₃N₄ for the degradation of methyl orange under simulated sunlight irradiation. *J. Alloys Compd.* **2015**, *622*, 1098–1104.
- (104) Onwudiwe, D. C.; Olatunde, O. C.; Nkwe, V. M.; Smida, Y. B.; Ferjani, H. Dual S-scheme heterojunction g-C₃N₄/Bi₂S₃/CuS composite with enhanced photocatalytic activity for methyl orange degradation. *Inorg. Chem. Commun.* **2023**, *155*, No. 111075.
- (105) Li, S.; Wang, C.; Cai, M.; Yang, F.; Liu, Y.; Chen, J.; Zhang, P.; Li, X.; Chen, X. Facile fabrication of TaON/Bi₂MoO₆ core-shell S-scheme heterojunction nanofibers for boosting visible-light catalytic levofloxacin degradation and Cr (VI) reduction. *J. Chem. Eng.* **2022**, *428*, No. 131158.
- (106) Li, S.; Wang, C.; Liu, Y.; Cai, M.; Wang, Y.; Zhang, H.; Guo, Y.; Zhao, W.; Wang, Z.; Chen, X. Photocatalytic degradation of tetracycline antibiotic by a novel Bi₂Sn₂O₇/Bi₂MoO₆ S-scheme heterojunction: performance, mechanism insight and toxicity assessment. *J. Chem. Eng.* **2022**, *429*, No. 132519.
- (107) Li, S.; Wang, C.; Cai, M.; Liu, Y.; Dong, K.; Zhang, J. Designing oxygen vacancy mediated bismuth molybdate (Bi₂MoO₆)/N-rich carbon nitride (C₃N₃) S-scheme heterojunctions for boosted photocatalytic removal of tetracycline antibiotic and Cr (VI): Intermediate toxicity and mechanism insight. *J. Colloid Interface Sci.* **2022**, *624*, 219–232.